Effects of scatterers' sizes on near-field coherent anti-Stokes Raman scattering under tightly focused radially and linearly polarized light excitation

Jian Lin[1], Wei Zheng[1], Haifeng Wang[2], and Zhiwei Huang[1,*]

[1]*Bioimaging Laboratory, Department of Bioengineering, Faculty of Engineering, National University of Singapore, Singapore 117576, Singapore*
[2]*A*star, Data Storage Institute, DSI Building, 5 Engineering Drive 1, Singapore 117608, Singapore*
**biehzw@nus.edu.sg*

Abstract: We employ the finite-difference time-domain (FDTD) technique as a numerical approach to studying the effects of scatterers' sizes on near-field coherent anti-Stokes Raman scattering (CARS) microscopy under tightly focused radially and linearly polarized light excitations. The FDTD results show that in a uniform medium (water), the full width at half maximum (FWHM) (transverse resolution) of radially polarized near-field CARS (RP-CARS) radiation is approximately 7.7% narrower than that of linearly polarized near-field CARS (LP-CARS) imaging, whereas the depth of focus (DOF) of RP-CARS radiation is 6.5% longer than LP-CARS. However, with the presence of scatterers in the uniform medium, both the FHWM and DOF of near-field RP-CARS radiation become much narrower compared to those of near-field LP-CARS radiation. In addition, the signal to nonresonant background ratio of near-field RP-CARS is significantly improved when the scatterer's size is larger than a half wavelength of the pump light field. This work suggests that near-field CARS radiations are strongly influenced by the scatterers' sizes in the medium; and near-field RP-CARS microscopy is superior to the near-field LP-CARS by providing both higher transverse and axial resolutions for three-dimensional molecular imaging of fine structures in biological systems.

OCIS codes: (180.6900) Three-dimensional microscopy; (290.5850) Scattering, particles; (260.5430) Polarization; (300.6230) Spectroscopy, coherent anti-Stokes Raman scattering.

References and links

1. A. Zumbusch, G. R. Holtom, and X. S. Xie, "Three-dimensional vibrational imaging by coherent anti-Stokes Raman scattering," Phys. Rev. Lett. **82**(20), 4142–4145 (1999).
2. C. L. Evans, X. Xu, S. Kesari, X. S. Xie, S. T. C. Wong, and G. S. Young, "Chemically-selective imaging of brain structures with CARS microscopy," Opt. Express **15**(19), 12076–12087 (2007).
3. F. Lu, W. Zheng, and Z. Huang, "Heterodyne polarization coherent anti-Stokes Raman scattering microscopy," Appl. Phys. Lett. **92**(12), 123901 (2008).
4. X. Nan, E. O. Potma, and X. S. Xie, "Nonperturbative chemical imaging of organelle transport in living cells with coherent anti-stokes Raman scattering microscopy," Biophys. J. **91**(2), 728–735 (2006).
5. F. Lu, W. Zheng, C. Sheppard, and Z. Huang, "Interferometric polarization coherent anti-Stokes Raman scattering (IP-CARS) microscopy," Opt. Lett. **33**(6), 602–604 (2008).
6. N. Djaker, D. Gachet, N. Sandeau, P. F. Lenne, and H. Rigneault, "Refractive effects in coherent anti-Stokes Raman scattering microscopy," Appl. Opt. **45**(27), 7005–7011 (2006).
7. C. Liu, Z. Huang, F. Lu, W. Zheng, D. W. Hutmacher, and C. Sheppard, "Near-field effects on coherent anti-Stokes Raman scattering microscopy imaging," Opt. Express **15**(7), 4118–4131 (2007).
8. V. V. Krishnamachari, and E. O. Potma, "Focus-engineered coherent anti-Stokes Raman scattering microscopy: a numerical investigation," J. Opt. Soc. Am. A **24**(4), 1138–1147 (2007).

#122196 - $15.00 USD Received 4 Jan 2010; revised 16 Mar 2010; accepted 12 Apr 2010; published 10 May 2010

9. J. Lin, H. Wang, W. Zheng, F. Lu, C. Sheppard, and Z. Huang, "Numerical study of effects of light polarization, scatterer sizes and orientations on near-field coherent anti-Stokes Raman scattering microscopy," Opt. Express **17**(4), 2423–2434 (2009).
10. H. Wang, L. Shi, B. Lukyanchuk, C. Sheppard, and C. T. Chong, "Creation of a needle of longitudinally polarized light in vacuum using binary optics," Nat. Photonics **2**(8), 501–505 (2008).
11. F. Lu, W. Zheng, and Z. Huang, "Coherent anti-Stokes Raman scattering microscopy using tightly focused radially polarized light," Opt. Lett. **34**(12), 1870–1872 (2009).
12. R. Dorn, S. Quabis, and G. Leuchs, "Sharper focus for a radially polarized light beam," Phys. Rev. Lett. **91**(23), 233901 (2003).
13. L. Novotny, M. R. Beversluis, K. S. Youngworth, and T. G. Brown, "Longitudinal field modes probed by single molecules," Phys. Rev. Lett. **86**(23), 5251–5254 (2001).
14. K. Yoshiki, K. Ryosuke, M. Hashimoto, T. Araki, and N. Hashimoto, "Second-harmonic-generation microscope using eight-segment polarization-mode converter to observe three-dimensional molecular orientation," Opt. Lett. **32**(12), 1680–1682 (2007).
15. S. Yang, and Q. Zhan, "Third-harmonic generation microscopy with tightly focused radial polarization," J. Opt. A, Pure Appl. Opt. **10**(12), 125103 (2008).
16. J. X. Cheng, and X. S. Xie, "Green's function formulation for third-harmonic generation microscopy," J. Opt. Soc. Am. B **19**(7), 1604–1610 (2002).
17. Y. Saito, M. Motohashi, N. Hayazawa, M. Iyoki, and S. Kawata, "Nanoscale characterization of strained silicon by tip-enhanced Raman spectroscope in reflection mode," Appl. Phys. Lett. **88**(14), 143109 (2006).
18. K. S. Yee, "Numerical solution of initial boundary value problem involving Maxwell equations in isotropic media," IEEE Trans. Antenn. Propag. **14**(3), 302–307 (1966).
19. A. Volkmer, "Vibrational imaging and microspectroscopies based on coherent anti-Stokes Raman scattering microscopy," J. Phys. D Appl. Phys. **38**(5), R59–R81 (2005).
20. K. Takeda, Y. Ito, and C. Munakata, "Simultaneous measurement of size and refractive index of a fine particle in flowing liquid," Meas. Sci. Technol. **3**(1), 27–32 (1992).
21. B. Richards, and E. Wolf, "Electromagnetic diffraction in optical systems. II. Structure of the image field in an aplanatic system," Proc. R. Soc. Lond. A Math. Phys. Sci. **253**(1274), 358–379 (1959).
22. D. Courjon, and C. Bainier, "Near field microscopy and near field optics," Rep. Prog. Phys. **57**(10), 989–1028 (1994).
23. B. Jia, X. Gan, and M. Gu, "Direct observation of a pure focused evanescent field of a high numerical aperture objective lens by scanning near-field optical microscopy," Appl. Phys. Lett. **86**(13), 131110 (2005).
24. R. D. Schaller, J. Ziegelbauer, L. F. Lee, L. H. Haber, and R. J. Saykally, "Chemically selective imaging of subcellular structure in human hepatocytes with coherent anti-stokes Raman scattering (CARS) near-field scanning optical microscopy (NSOM)," J. Phys. Chem. B **106**(34), 8489–8492 (2002).
25. S. Kawata, Y. Inouye, and T. Ichimura, "Near-field optics and spectroscopy for molecular nano-imaging," Sci. Prog. **87**(1), 25–49 (2004).

1. Introduction

Coherent anti-Stokes Raman scattering (CARS) microscopy has received much interest for imaging tissue and cells owing to its outstanding capabilities of high biochemical selectivity and sensitivity, as well as its intrinsic three-dimensional (3-D) optical sectioning ability with high spatial and spectral resolutions [1–3]. Most CARS experiments and simulations utilize linearly polarized excitation light fields [3–9]. Very recently, radially polarized laser beams have attracted increasing attention because of their unique light distribution properties (e.g., a very strong longitudinal field component and a tighter focal spot size) in the focal region after being tightly focused by a high numerical aperture (NA) objective [10–12]. The unique radial focal field distribution thus has potential applications in high-resolution 3-D microscopy imaging, such as confocal microscopy [13], second harmonic generation (SHG) [14], third harmonic generation (THG) [15], and CARS microscopy [11]. Although the radially polarized CARS (RP-CARS) microscopy has been proven to be in favor of revealing longitudinally oriented molecules [11], the near-field distributions of RP-CARS radiation compared to linearly polarized CARS (LP-CARS) have yet been investigated in details.

A number of simulation work based on geometric optics and wave optics, as well as the vectorial theory have shown that refractive index mismatch and focal-field distribution have significant effects on the far-field CARS generation [6,8]. Our recent studies [7,9] on near-field CARS microscopy using the finite-difference time-domain (FDTD) method also indicates that the excitation field distributions and intensities of near-field CARS signals are substantially altered by small scatterers due to index mismatch in the medium. But the generation of

#122196 - $15.00 USD Received 4 Jan 2010; revised 16 Mar 2010; accepted 12 Apr 2010; published 10 May 2010

near-field CARS signals strongly depends on the polarization direction of the excitation light field as shown in our previous results [9]. In the cases of CARS studies on small structures in cells or intracellular organelles, if the physical size of targets of interest (e.g., mitochondria, membranes) is equivalent to or even smaller than the wavelength of excitation light used, it is expected that the evanescent waves generated due to the near-field effects could dominate the local light fields within the molecule, and vary with a number of near-field factors such as the refractive index mismatch, edge effect, surface roughness, etc [16–18], which will significantly affect the CARS signal generations [7,9]. Hence, the near-field effects should be taken into account in CARS microscopy particularly on nano-molecular imaging. In this paper, we employ the FDTD technique to study the effect of nanoparticles' sizes on the near-field distributions of RP-CARS and LP-CARS radiation under tightly focused radially and linearly polarized light excitation, and also compare the spatial resolution (transverse and axial resolutions) between the near-field RP-CARS and LP-CARS microscopy.

2. Methods

Figure 1 shows the schematic of the RP-CARS or LP-CARS field (E_{CARS}) generation in FDTD simulations, in which the radially or linearly polarized pump (E_p) and Stokes (E_s) light beams are tightly focused onto a spherical nano-scatterer (e.g., polystyrene beads) by passing through a high numerical aperture water immersion microscope objective (NA = 1.2).

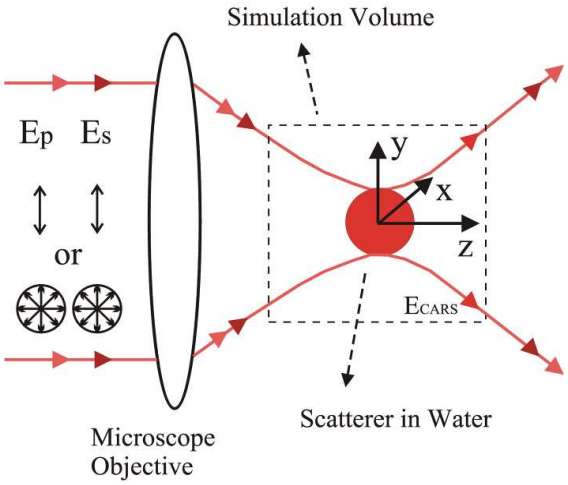

Fig. 1. Schematic of near-field LP-CARS or RP-CARS field (E_{CARS}) generation under tightly focused linearly polarized (e.g., y-polarized) or radially polarized pump (E_p) and Stokes (E_s) light fields through a high NA objective. LP-CARS, linearly polarized CARS; RP-CARS, radially polarized CARS. The calculation volume was divided into cubic cells of $\lambda_p/40$ at each step, where λ_p (750 nm) is the pump beam wavelength, and the wavelength of Stokes beam λ_s is chosen to be 852 nm, and then the generated CARS signal is at 670 nm, representing a resonant Raman shift of 1600 cm^{-1} of mono-substituted benzene rings stretching vibrations in polystyrene beads [19]. The refractive indices of the scatterer (polystyrene beads) and surrounding medium (water) are assumed to be 1.59 and 1.33, respectively [20].

For a tightly focused linearly polarized laser beam, the focal field distribution in cylindrical coordinates can be expressed as [21]:

$$\mathbf{E}(\rho,\varphi,z) = -iA\begin{bmatrix} I_0 + I_2\cos 2\varphi \\ I_2 \sin 2\varphi \\ 2I_1 \cos\varphi \end{bmatrix}, \quad (1)$$

#122196 - $15.00 USD Received 4 Jan 2010; revised 16 Mar 2010; accepted 12 Apr 2010; published 10 May 2010

where A is a real constant; $\rho = \sqrt{x^2 + y^2}$, φ is the azimuthal angle and I_n is given by

$$I_n = \int_0^{\alpha} e^{-\sin^2\theta/\sin^2\alpha} \sin\theta \cos^{1/2}(\theta) g_n(\theta) J_n(k\rho\sin\theta) e^{ikz\cos\theta} \mathrm{d}\theta, \quad (2)$$

where $g_n(\theta)$ equals, $(1+\cos\theta)$ and $(1-\cos\theta)$ for n = 0, 1, 2, respectively; J_n is the first kind Bessel function of order n; $k = 2\pi n/\lambda$ is the wave vector (n is the refractive index of the medium), and $\alpha = \arcsin(\mathrm{NA}/n)$.

The longitudinal electric field component (E_z) and the radial component (E_ρ) in the focal region of a tightly focused radially polarized Bessel-Gaussian beam can be expressed as [10]:

$$E_z(\rho, z) = 2iA\int_0^{\alpha} \cos^{1/2}(\theta)\sin^2(\theta) l(\theta) J_0(k\rho\sin\theta) e^{ikz\cos\theta} \mathrm{d}\theta, \quad (3)$$

$$E_\rho(\rho, z) = 2A\int_0^{\alpha} \cos^{1/2}(\theta)\sin(2\theta) l(\theta) J_1(k\rho\sin\theta) e^{ikz\cos\theta} \mathrm{d}\theta, \quad (4)$$

where the parameters are same as in Eqs. (1), (2) except that $l(\theta)$ is the pupil function of a Bessel-Gaussian beam [10]:

$$l(\theta) = \exp\left[-\beta_0^2\left(\frac{\sin\theta}{\cos\alpha}\right)^2\right] J_1\left(2\beta_0\frac{\sin\theta}{\sin\alpha}\right), \quad (5)$$

where $\beta_0 = 3/2$ is the ratio of the pupil radius to the beam waist.

We apply the finite-difference time-domain (FDTD) technique [18] to solve Maxwell's equations directly in time domain through the leap-frogging scheme [7,9] for computing the field distributions, e.g., pump field [$\mathbf{E}(\mathbf{r}, \omega_p)$], Stokes field [$\mathbf{E}(\mathbf{r}, \omega_s)$], and CARS field [$\mathbf{E}(\mathbf{r}, \omega_{as})$] of the tightly focused radially polarized pump and Stokes fields near the focal point of the microscope objective by incorporating the Eqs. (1)–(5) into the FDTD program developed [9]. Then the induced third-order nonlinear polarization at the anti-Stokes frequency, $\omega_{as} = 2\omega_p - \omega_s$, can be calculated by [7,9]:

$$P_i^{(3)}(\mathbf{r}, \omega_{as}) = 3\sum_{jkl} \chi_{ijkl}^{(3)} E_j(\mathbf{r}, \omega_p) E_k(\mathbf{r}, \omega_p) E_l^*(\mathbf{r}, \omega_s), \quad (6)$$

where $\chi_{ijkl}^{(3)}$ is the third-order nonlinear susceptibility; i, j, k, and l run over x, y, z, respectively.

3. Results and Discussion

Figure 2 shows the near-field intensity distributions of RP-CARS (a) and LP-CARS (b) generated from pure water in the y-z plane. The intensity profiles along the lateral direction [Fig. 2(c)] show that the full width at half maximum (FWHM) of RP-CARS radiation is 272 nm, which is 7.7% narrower than LP-CARS (FWHM of 293 nm). This indicates the advantage of RP-CARS microscopy for providing higher transverse resolution for molecular imaging. The above is consistent with our analytical results in RP-CARS imaging [11], showing the reliability of our FDTD method for CARS simulation. We also compare the depth of focus (DOF) between RP-CARS and LP-CARS radiations [Fig. 2(d)]. RP-CARS radiation at the focal region has a 6.5% longer DOF than LP-CARS (DOF of 984 nm). Although the above results are calculated in a uniform medium (i.e., water), they will also be valid for other uniform bulky media with the scatterers' sizes being much larger than the focal spot size.

#122196 - $15.00 USD Received 4 Jan 2010; revised 16 Mar 2010; accepted 12 Apr 2010; published 10 May 2010

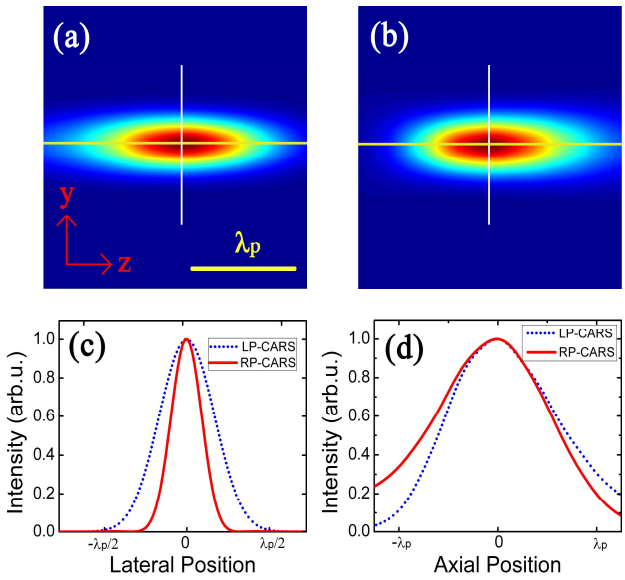

Fig. 2. Comparison of near-field CARS intensity distributions in the y-z plane between the RP-CARS (z-component) (a) and the LP-CARS (y-component) (b) generated from pure water. Comparison of the intensity profiles of RP-CARS and LP-CARS in the lateral (c) and axial (d) directions along the corresponding lines indicated in Figs. 2(a) and 2(b).

Figure 3 shows the near-field intensity distributions of RP-CARS and LP-CARS for the scatterers in water with diameters of (a) $0.1\lambda_p$; (b) $0.25\lambda_p$; (c) $0.5\lambda_p$; (d) $0.75\lambda_p$; and (e) $1.0\lambda_p$, respectively. The first and third panels represent the intensity distributions in the y-z plane for RP-CARS and LP-CARS, respectively. The corresponding intensity profiles along the axial direction are shown in the second and fourth panels. The maximum intensity of RP-CARS radiation increases rapidly with the increased sizes of scatterers, reaching to 120 times of that in pure water (second panel of Fig. 3). This is probably due to the reasons that the excitation light tends to be more focused onto larger nanoparticles, leading to a stronger light field distributions inside larger nanoparticles than those in smaller scatterers [9]. In addition, the conservation of the electric displacement **D** in the polarization (z) direction also leads to an enhanced electric field adjacent to the nanoparticle-water interface [22]. The intensity enhancements at both of the nanoparticle-water interfaces along z direction for small scatterers ($D \leq 0.5\lambda_p$) could be attributed to the near-field enhancements (e.g., the generation of the non-propagating evanescent field [7,9,22], which decreases rapidly with the increased scatterers' sizes [7,9]. Similar phenomena can also be observed in LP-CARS, i.e., enhanced signals at the nanoparticle-water interfaces along the polarization (y) direction for small scatterers ($D \leq 0.5\lambda_p$), and the increase of intensity with increased scatterers' sizes (fourth panel of Fig. 3); however, the maximum enhancement factor of LP-CARS intensity is 20, which is only 1/6 of that in RP-CARS radiation. These results show that near-field RP-CARS microscopy is more sensitive to the nanoparticle-water interface, which could be in favor of revealing the fine structures of biological samples.

#122196 - $15.00 USD Received 4 Jan 2010; revised 16 Mar 2010; accepted 12 Apr 2010; published 10 May 2010

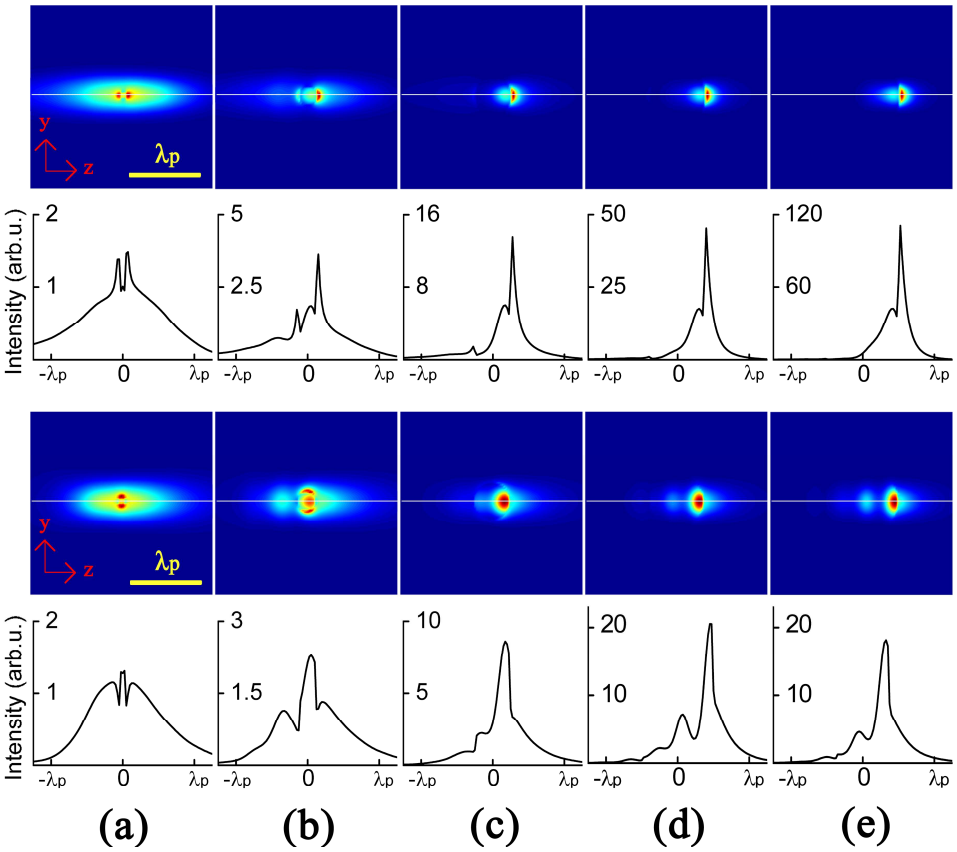

Fig. 3. Near-field intensity distributions of RP-CARS and LP-CARS for scatterers with diameters of (a) $0.1\lambda_p$; (b) $0.25\lambda_p$; (c) $0.5\lambda_p$; (d) $0.75\lambda_p$; and (e) $1.0\lambda_p$, respectively. The first and third panels represent the intensity distributions in the y-z plane for RP-CARS and LP-CARS, respectively. The corresponding intensity profiles along the white lines in the first and third panels of Fig. 3 are plotted in the second and fourth panels, respectively.

Figure 4 compares the FWHM and DOF between RP-CARS and LP-CARS radiations in water alone, and in water and scatterers with different sizes (D = $0.1\lambda_p$, $0.25\lambda_p$, $0.5\lambda_p$, 0.75, and $1.0\lambda_p$). Obviously, the transverse resolution of RP-CARS is much narrower than LP-CARS in both situations (i.e., with water alone, and with water and scatterers), giving a minimum value of 127 nm (D = $0.25\lambda_p$), which is 23% narrower than LP-CARS and 47% of that with water alone [Fig. 4(a)]. The relatively large FWHM of LP-CARS in Fig. 4(a) with scatterer's size of $0.25\lambda_p$ is due to the near-field enhancements at the upper and lower surfaces of the scatterer [7,9] [third panel of Fig. 3(b)], which broadens the field distributions along the y-direction. Different from FWHM, the DOF of RP-CARS is smaller than LP-CARS only when the scatterers exist in the light propagation medium, and the value decreases down to 67 nm (D = $0.5\lambda_p$), which is 39% shorter than LP-CARS and 6% only of that with water alone [Fig. 4(b)]. These results indicate that the nano-scatterers in medium significantly reduce the focal spot volume in both longitudinal and transverse directions in RP-CARS and LP-CARS microscopy. However, this narrowing effect of CARS radiation becomes more prominent in RP-CARS microscopy, illustrating the advantages of RP-CARS to provide both higher transverse and longitudinal resolutions, particularly suited for three-dimensional imaging of fine cellular structures in biological systems.

#122196 - $15.00 USD Received 4 Jan 2010; revised 16 Mar 2010; accepted 12 Apr 2010; published 10 May 2010

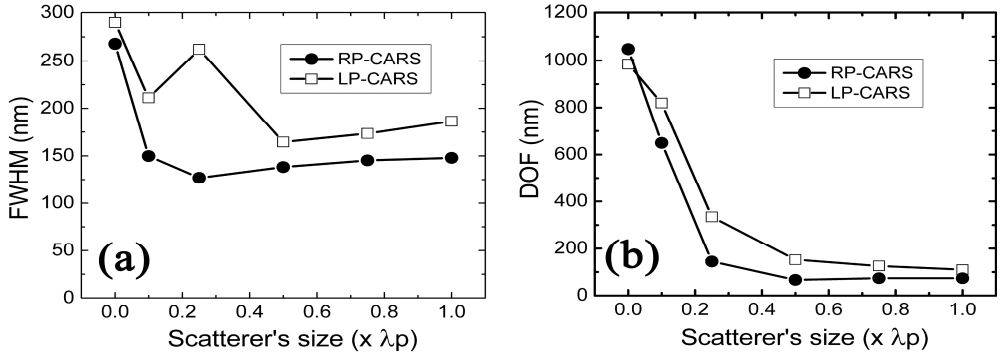

Fig. 4. The full width at half maximum (FWHM) (a) and the depth of focus (DOF) (b) of RP-CARS and LP-CARS with water alone, and with water and scatterers in different sizes (D = $0.1\lambda_p$, $0.25\lambda_p$, $0.5\lambda_p$, 0.75, and $1.0\lambda_p$). Note that the values at zero scatterer's size means the scattering medium is pure water.

Figure 5 shows the signal to background ratios (SBR) of near-field RP-CARS and LP-CARS radiations with different scatterers' sizes (D = $0.1\lambda_p$, $0.25\lambda_p$, $0.5\lambda_p$, 0.75, and $1.0\lambda_p$). The SBR of RP-CARS increases rapidly with the increased scatterers' sizes (up to 225 when the scatterer is $1.0\lambda_p$). This is probably due to the fact that RP-CARS radiation tends to be more concentrated in the forward direction for larger scatterers [first panel of Figs. 3(c)–3(e)], resulting in a sharp and intense peak centered at the water-scatterer interface [second panel of Figs. 3(c)–3(e)]. However, the SBR of LP-CARS remains nearly unchanged (fluctuating at around 40) with the increased scatterers' sizes, and this is due to the more diffuse near-field distributions of LP-CARS with larger scatterers [third panel of Figs. 3(c)–3(e)]. It is also observed that when the scatterer's size is larger than a half wavelength of the pump light field, near-field RP-CARS radiation has a much higher SBR than LP-CARS; whereas the converse is valid when the scatterer's size is smaller than the half wavelength of the pump light field. Hence, near-field LP-CARS microscopy provides a better contrast for imaging the smaller scatterers ($D<0.5\lambda_p$); while for the larger scatterers, near-field RP-CARS microscopy provides much higher contrast of image with higher spatial resolutions.

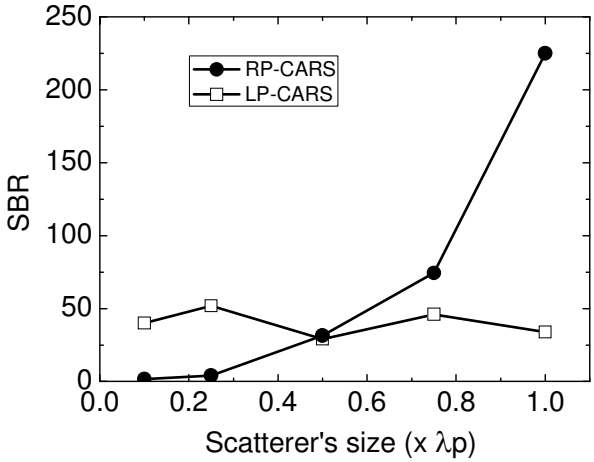

Fig. 5. Comparison of signal to background ratios (SBR) of RP-CARS and LP-CARS versus scatterers' sizes (D = $0.1\lambda_p$, $0.25\lambda_p$, $0.5\lambda_p$, 0.75, and $1.0\lambda_p$).

In this work, we applied the advanced numerical technique - finite-difference time-domain (FDTD) method to numerically resolve the Maxwell equations without the need of boundary conditions for investigating the effects of scaterers' sizes on near-field RP-CARS and

#122196 - $15.00 USD Received 4 Jan 2010; revised 16 Mar 2010; accepted 12 Apr 2010; published 10 May 2010

LP-CARS radiations. The simulation results show that near-field CARS radiations are strongly influenced by the scatterers in the light propagation medium. With the presence of scatterers in water, the SBR of near-field RP-CARS can reach up to 220, which is 4.5 times higher than near-field LP-CARS (Fig. 5). The FWHM and DOF of RP-CARS and LP-CARS decrease due to the existence of scatterers in the medium, resulting in the reduced focal spot sizes of 127 nm and 164 nm in the transverse direction as well a shorter focal length of 67 nm and 110 nm, respectively (Fig. 4). Therefore, near-field radially polarized CARS microscopy has a great potential of providing higher contrast and higher axial and transverse resolutions in three-dimensional imaging of fine cellular structures in biological systems. One notes that the near-field distributions and near-field CARS imaging could be directly mapped out by using near-field detection schemes, such as near-field scanning optical microscopy (NSOM) [22–24], and nonlinear optics (e.g., tip-enhanced CARS microscopy) [17,25], which can realize vibrational imaging of nanostructures far beyond the spatial resolution of far-field CARS microscopy.

Acknowledgments

This work was supported by the Biomedical Research Council, the National Medical Research Council, and the Faculty Research Fund from the National University of Singapore.

#122196 - $15.00 USD Received 4 Jan 2010; revised 16 Mar 2010; accepted 12 Apr 2010; published 10 May 2010